

Adaptive subcarrier intensity modulation for free space optical communication

Mike S. Ferraro,^{a,*} Rita Mahon,^a William S. Rabinovich,^a
Andrew G. Coffee,^b James L. Murphy,^a James L. Dexter,^a
and Wade T. Freeman^c

^aU.S. Naval Research Laboratory, Washington, DC, United States

^bJacobs Corporation, Hanover, Maryland, United States

^cSmart Logic, Inc., Vienna, Virginia, United States

Abstract. Increased capacity demands and radio frequency (RF) congestion impacts on current communication networks have brought greater attention to free-space optical (FSO) communication as a viable augmentation technology for terrestrial, aerial, and space-based communication infrastructure. As a complementary alternative to RF communication systems, FSO can support high link bandwidths and provide high data security without RF spectral constraints. The performance of FSO links, however, can be significantly impacted by receive power variation caused by propagation and scattering losses along with losses due to atmospheric turbulence. Depending on the FSO application, these loss mechanisms can dynamically change, impacting link performance at different time scales. We investigate subcarrier phase-shift keying (PSK) and quadrature amplitude modulation (QAM) intensity modulation that can be adapted to dynamically changing link conditions to optimize bandwidth utilization. Using custom subcarrier intensity modulation (SIM) modems, the performance of binary PSK (BPSK), QPSK, 8PSK, 16APSK, and 16-QAM waveforms is reported. The impact of adaptive equalization is also characterized, and the initial performance of a subcarrier multiplexed system is presented. This work represents the first experimental evaluation of SIM waveforms using a laboratory scintillation playback system based on scintillation recorded over real-world propagation paths. © The Authors. Published by SPIE under a Creative Commons Attribution 4.0 International License. Distribution or reproduction of this work in whole or in part requires full attribution of the original publication, including its DOI. [DOI: [10.1117/1.OE.61.6.066105](https://doi.org/10.1117/1.OE.61.6.066105)]

Keywords: free-space optical communication; subcarrier intensity modulation; optical scintillation.

Paper 20210784 received Jul. 21, 2021; accepted for publication May 24, 2022; published online Jun. 16, 2022.

1 Introduction

The growth of global connectivity and capacity demands has driven the need for expanding communication network capabilities to incorporate resilient alternative communication approaches to complement radio-frequency (RF)-based systems. Owing to its ability to support high data rates, maintain a high level of data security, and require no frequency allocation, free-space optical (FSO) communication represents a viable augmentation technology to current RF approaches. Despite these advantages, the dynamic nature of the atmospheric propagation channel can detrimentally impact FSO link performance. Atmospheric turbulence imposes intensity and phase fluctuations on the propagating beam, causing temporal and spatial variations at the receiver. For terrestrial FSO applications, channel conditions can change dynamically from a low turbulence regime to high turbulence based on a number of atmospheric and meteorological parameters over land and water.^{1,2} As turbulence increases, the temporal scale of turbulence-induced fades and surges can range from a few milliseconds to tens of milliseconds and cause receive power variation in excess of 20 dB. Propagation and scattering losses also impact FSO link performance. While geometric propagation losses for a fixed point-to-point terrestrial link are relatively

*Address all correspondence to Mike S. Ferraro, mike.ferraro@nrl.navy.mil

constant, this is not the case for air-to-ground and space-to-ground links. For instance, low Earth orbit (LEO)-to-ground FSO links can incur >10 -dB power variation from propagation and scattering losses over an LEO pass in addition to >10 dB from turbulence impacts. While the time-scale of turbulence effects is on the order of milliseconds, propagation and scattering losses are slower, with a timescale of minutes. The link margin for a given FSO-LEO pass can change by 20 dB as the pass progresses from low to high elevation angles. Maximizing data throughput in these dynamic link conditions involves accommodating for low signal-to-noise ratio (SNR) in high atmospheric loss conditions, where a more power-efficient modulation technique would be preferred, and high SNR in low atmospheric loss conditions, where power efficiency could be sacrificed for increased bandwidth efficiency. Research in dynamically optimizing FSO link performance includes investigating available modulation formats in tandem with error-correction techniques.^{3–10}

Numerous modulation techniques have been extensively investigated for FSO links including intensity-modulated direct-detection (IM/DD) on-off-keying (OOK) and pulse-position-modulation (PPM). OOK is attractive for its implementation simplicity but does not allow for increased bandwidth utilization when SNR is high. While PPM offers excellent power efficiency and is often used in photon-starved FSO applications,^{11,12} its performance comes at the cost of reduced bandwidth. Another approach is subcarrier intensity modulation (SIM) using phase-shift keying (PSK) and quadrature amplitude modulation (QAM) waveforms. The simplest of these is binary phase-shift keying (BPSK) where the bit rate is equal to the symbol rate. Higher-order waveforms provide increased spectral or bandwidth efficiency and therefore, allow for the transmission of multiple bits per symbol. Quadrature phase-shift keying (QPSK), 8PSK, and 16-QAM can transmit two, three, and four bits/symbols, respectively. The increased bandwidth efficiency for these waveforms is offset by reduced power efficiency. QPSK, e.g., doubles the throughput of BPSK but requires 3 dB more RF signal power to maintain the same quality of service. In fiber-optic communication, multiorder waveforms like PSK and QAM most commonly have been implemented using an optically coherent waveform in which the encoding is relative to the optical phase. When the light illuminating the detector is in a single optical mode, this approach offers the highest bandwidth and best sensitivity. In an FSO system that includes an atmospheric path, turbulence will cause the received light to be multimode. In that case, optically coherent multiorder waveforms can still be used if adaptive optics or some other correction mechanism is implemented but at the cost of increased system complexity. In this work, we investigate an alternative approach: encoding QAM or PSK waveforms using SIM.^{13,14} The encoding in SIM is achieved with an RF tone placed on the optical beam. Relative to optically coherent approaches, SIM encoding is less efficient but is also less sensitive to optical turbulence since data decoding does not rely on recovered optical phase information. An adaptive approach incorporating SIM waveforms could dynamically match a particular waveform to the received signal power to optimize link throughput.

Waveform adaptation also allows for more efficient utilization of large-area avalanche photodiodes (APD). As compared with single-mode-fiber (SMF) coupled FSO systems, the main advantage of large area APDs for FSO links is in the relaxation of system pointing requirements for ground, aerial, and space-based terminals. Since these devices can be free-space coupled, receiver coupling optics are no longer constrained to the numerical aperture of SMF. Instead, low $f/\#$ optics can be used, producing larger fields-of-view (FOV). For example, a 100- μm active area photodetector, coupled with an $f/2$ collection optic, would increase the FOV by a factor of 20 relative to a SMF-based approach. A large area detector also allows for the coupling of light distorted by atmospheric turbulence, eliminating the need for adaptive optics commonly used in SMF-based systems.^{15,16} When fabricated in array form, these devices combine the functionality of position-sensitive detectors (PSDs) and data detectors in a single sensor, enabling more size, weight, and power (SWaP) efficient terminal design.^{17,18} A disadvantage of large area APDs is limited bandwidth response due to increased device capacitance. Relative to other modulation techniques such as OOK and PPM, an adaptive SIM approach can help optimize data throughput within the available bandwidth of these APDs when the received signal power is high.

SIM implementation can be accomplished in two ways: (1) through one large modulation channel within the available bandwidth or (2) through multiple appropriately spaced smaller

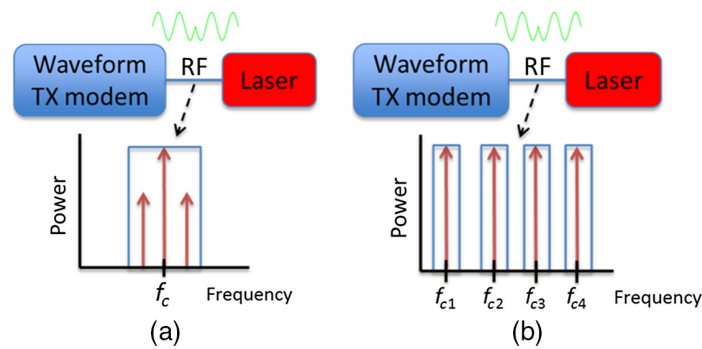


Fig. 1 SIM system architectures show: (a) a single modulation channel and (b) multiple modulation channels.

modulation channels via subcarrier multiplexing.^{19,20} Diagrams of the single and multichannel architectures are shown in Fig. 1. As a notional example, we consider an FSO link consisting of terminals using 150- μm diameter APD data detectors with bandwidth responses of ~ 1 GHz. Using one large modulation channel equal to the link bandwidth (i.e., 1 Gsymbol/s), we can achieve a throughput of 1 Gbps using BPSK in low SNR and 4 Gbps using 16-QAM or 16APSK in high SNR. Alternatively, four smaller modulation channels can be used, each with a 250-MHz bandwidth. The aggregated throughput, in this case, is the same as the large modulation scenario: 1 Gbps for BPSK and 4 Gbps for 16-QAM and 16APSK.

The availability of SIM waveforms for FSO is contingent on waveform performance as a function of received power under the dynamic scintillation conditions present for a particular FSO link. While significant theoretical work has been done to simulate SIM waveform performance under optical scintillation^{21–26} using well-known optical propagation models,²⁷ these models are sometimes inconsistent with scintillation response measured in the field and rely on models for component performance that may be idealized. Furthermore, this research does not evaluate higher-order SIM waveforms beyond 8PSK. Experimental studies can, in principle, avoid some of these limitations, but to date, have only evaluated the performance of subcarrier BPSK.^{13,28} Laboratory characterizations such as those reported in Ref. 28 are also based on scintillation simulators that may not be representative of observed atmospheric turbulence.

Rather than rely purely on atmospheric channel modeling, the U.S. Naval Research Laboratory (NRL) has developed a laboratory scintillation playback system for characterizing link performance under different scintillation conditions. Laboratory simulation of scintillation has often involved propagating light over distances much shorter than practical link ranges while using heaters and fans to produce thermal flows much stronger than what is observed in nature. Turbulence in the atmosphere is characterized by the atmospheric structure constant, C_n^2 . In natural atmospheres, C_n^2 typically varies from values of 10^{-16} to 10^{-12} $\text{m}^{-2/3}$. Laboratory simulators often use values of C_n^2 of 10^{-9} $\text{m}^{-2/3}$ or higher. This can produce variances in the signal that is of the order observed in long-range links. However, the effects of scintillation depend on more than just the signal variance. The detailed distribution function of surges and fades and the temporal behavior, measured by the power spectral density, are the critical measures of the effects of scintillation. Laboratory simulation does not necessarily reproduce these effects because it does not reproduce the effects of long-range optical propagation.

To accurately emulate scintillation in the laboratory, NRL has adopted a different approach. A free-space optical link using two terminals is set up on a test range many kilometers in length. The transmit terminal sends out a continuous wave beam. The fluctuations of the signal strength at the receiver terminal are measured using a high dynamic range photodetector with kHz bandwidth. It is then digitized and stored. Recordings of scintillation under a wide variety of environmental conditions are collected providing a library of real-world scintillation behavior that can be played back in the laboratory. This approach guarantees that the statistical properties of the scintillation are accurate, and it has not only proven effective in testing and optimizing system components such as photodetectors but also in evaluating error-correction techniques such

as data transmission temporal diversity and adaptive low-density parity check (LDPC) coding.^{29,30}

In Sec. 2 of this paper, we discuss the development of SIM waveform modems and the test-bed incorporating the scintillation playback system. Section 3 describes the testing of a single channel SIM architecture and the performance of BPSK, QPSK, 8PSK, 16APSK, and 16-QAM waveforms under various scintillation profiles. The implementation and impact of adaptive equalization on modem performance are also described and compared with modeled waveform response. To convey the benefit of an adaptive SIM waveform approach for FSO applications, the presented waveform characterization data is used to predict waveform availability for a FSO-LEO downlink scenario using an NRL-developed link analysis tool.³¹ Finally, in Sec. 4, initial waveform measurements using a subcarrier multiplexed system are discussed.

2 SIM Modem and Laboratory Test-Bed Development

SIM waveform modems were developed using two Xilinx FPGA platforms: the Virtex-5 and the Kintex 7. Each platform incorporates commercial off-the-shelf high data rate modulator (HDRM-M) and high data rate demodulator (HDRM-D) IP cores developed by Silicon Infusion. Custom I/Q modulator and demodulator interface electronics were designed for both modem types. An Ethernet interface for packet-error-rate (PER) testing along with an integrated waveform constellation monitor are common to both designs. The Virtex-5 platform supports a selectable carrier frequency and symbol rates up to 40 Msym/s for PSK and QAM waveforms. The symbol rate in this case is limited by the FPGA clock frequency rather than the IP core. Power consumption is ~ 7 W. The motivation for use of the Virtex-5 is its demonstrated radiation hardness for space applications.

Although the Kintex-7 can support symbol rates in excess of 100 Msym/s, the reference design and associated up-converter utilized for this research limit the symbol rate to ~ 50 Msym/s. Contrary to the Virtex-5, the Kintex-7 is not space-qualified. However, a future variant of this modem could be designed using the newer generation Kintex Ultrascale which is a space-grade platform that provides enhanced performance while reducing power consumption. The 15-W power consumption of the current Kintex-7 platform is based on the Xilinx reference design which includes functionality not required for this application. Power consumption for a custom design based on the Kintex Ultrascale would be less than that of the Virtex-5 modem.

Waveform performance was characterized using a laboratory test-bed with an integrated scintillation playback system as shown in Fig. 2. The transmit modem intensity modulates a laser transmitter through a low noise amplifier with 26 dB RF gain and a low-pass filter. For this testing, a single modulation channel spans a bandwidth of 40 MHz, centered at 115 MHz. The laser transmitter consists of a 1550-nm CW laser mated to a lithium-niobate optical modulator with an extinction ratio >20 dB. It provides the input to an acousto-optic modulator (AOM), a key component of the scintillation playback system. The AOM provides a dynamic range of >35 dB, allowing for representative playback of measured irradiance files which often show signal variation >20 dB. The output power of the AOM is controlled using a variable optical attenuator (VOA), which is then coupled to a fiber focuser. The fiber focuser produces a $50\text{-}\mu\text{m}$ spot size at a working distance of 21 mm. The data photodetector used for this testing is the center element of a $265\text{-}\mu\text{m}$ diameter, concentric impact ionization engineered APD array. The active diameter of the center element of the APD array is $\sim 112\ \mu\text{m}$. While the center element is capable of bandwidths beyond 1 GHz, the corresponding data detector front-end amplifier was optimized for a 3-dB bandwidth of ~ 165 MHz. The front-end design includes an automatic gain control (AGC) loop which provides a dynamic range in excess of 40 dB. Using 155 Mbps OOK, a detector sensitivity of -49.7 dBm, or ~ 520 photons/bit, was measured at $\sim 10^{-9}$ bit-error-rate.³² Despite the lower bandwidth response of the front-end electronics, the single modulation channel used for testing occupies less than one-third of the data detector bandwidth. More efficient utilization of this detector bandwidth will be addressed in the development of a subcarrier multiplexed system, described in a later section. The detector output is then low-pass filtered and coupled to the receive modem for carrier and data recovery.

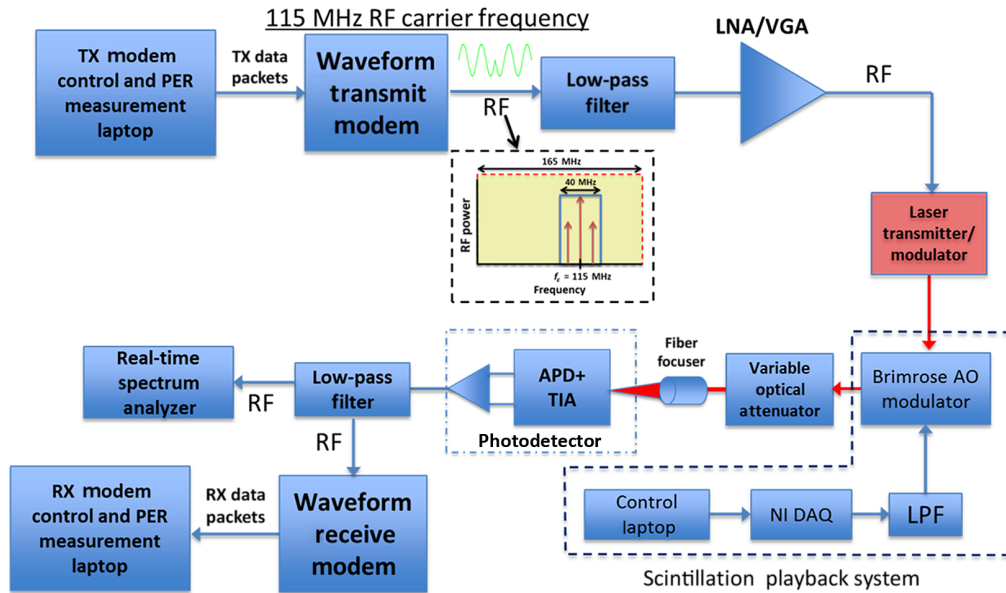


Fig. 2 Laboratory characterization test-bed with integrated scintillation playback system.

Simultaneously, the waveform constellation of the receive signal is monitored using both the modem constellation monitor and a real-time spectrum analyzer.

The scintillation playback system is based on the recording of transmitted irradiance data obtained in real atmospheric environments, and the subsequent ability to replay those conditions in a laboratory setting. The intensity response recorded in each file corresponds to a scintillation index, σ_I^2 , which is a measure of observed irradiance variance. NRL has a range of recorded files at each site, varying from low to high scintillation indices. Here, we use files recorded on a 4-km long test range at Fort AP Hill, Virginia, United States. The beam path was about 8 m above the ground, and the receive aperture was 5 cm. Three such files with $\sigma_I^2 = 0.2, 0.6, \text{ and } 1.25$, were used for the waveform testing reported here and correspond to low, moderate, and high scintillation channel conditions. Files were played back using a custom Labview application and a National Instruments (NI) data acquisition (DAQ) module. The low-pass filtered output of the NI DAQ drives the AOM. Prior to playback, files are normalized such that the highest surge in a file corresponds to the most transmissive state of the AOM.

3 Single Channel SIM System Performance Characterization

3.1 Waveform Characterization Without Scintillation

Raw PER performance for each waveform, shown in Fig. 3, was characterized as a function of optical power at a symbol rate of 40 Msym/s. Initially, this was performed without scintillation playback where the AOM was intentionally set to its highest transmission level. The sharp increase in PER for a given waveform is bit-error dominated as the incident power is reduced to the detector noise floor. This is similar to the error response in fiber optic communication links. As the waveform complexity increases, the data throughput supported by a single 40 MHz modulation channel also increases but so does the power required to achieve a 1% PER. The supported data throughput and the optical power required to maintain 1% PER for each waveform are shown in Table 1. At 1% PER, BPSK provides a throughput of 40 Mbps at an optical power level of -51.5 dBm. QPSK doubles the throughput of BPSK at a 1% PER power of -50 dbm, a 1.5 dB increase in required optical power relative to BPSK. 8PSK and 16-QAM triple and quadruple the throughput of BPSK, respectively, but require 6.5 and 15 dB more power at 1% PER. Through more optimal modulator gain tuning, the performance of 16-QAM is ~ 1.5 dB better than previously reported.³³ 16APSK provides the same throughput as 16-QAM at a 1% PER power of -38.5 dBm, a 2 dB improvement over 16-QAM. Overall, this represents a

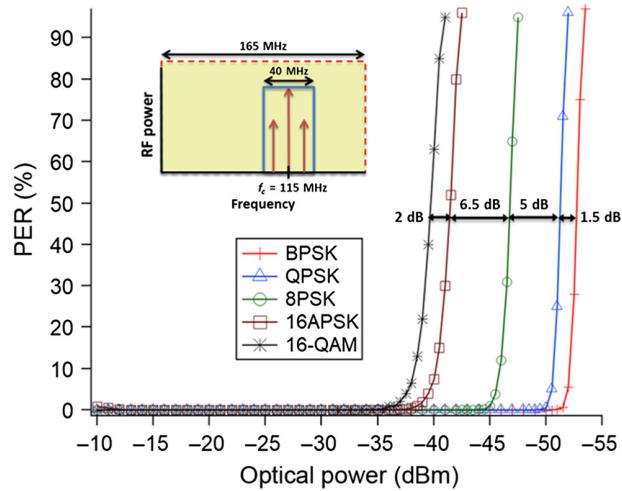


Fig. 3 PER performance as a function of optical power for BPSK, QPSK, 8PSK, 16APSK, and 16QAM waveforms without scintillation at a symbol rate of 40 Msym/s. As shown in the top-left inset figure, data were taken using a single modulation channel with a bandwidth of 40 MHz, centered at 115 MHz. The 3-dB bandwidth response of the data detector is ~ 165 MHz.

Table 1 Supported data throughput and optical power required to maintain 1% PER for BPSK, QPSK, 8PSK, 16APSK, and 16QAM waveforms at a symbol rate of 40 Msym/s.

| Waveform | Throughput (Mbps) | Optical power at 1% PER (dBm) |
|----------|-------------------|-------------------------------|
| BPSK | 40 | -51.5 |
| QPSK | 80 | -50 |
| 8PSK | 120 | -45 |
| 16APSK | 160 | -38.5 |
| 16QAM | 160 | -36.5 |

3.5-dB power efficiency improvement using a 4 bit/symbol waveform compared with prior work. Figure 4 shows a comparison of measured waveform performance relative to theoretical projections of PER response assuming an additive white Gaussian noise channel. BPSK and QPSK are within 1 dB of their projected performance while 8PSK is ~ 2.5 dB worse than expected. The largest performance discrepancies were observed for 16APSK and 16-QAM, which were 6 and 8 dB worse than expected, respectively. These discrepancies are due, in large part, to system component nonlinearities that detrimentally impact higher-order waveform performance. Leveraging well-established predistortion techniques for RF applications will be an area of future development to improve 16APSK and 16-QAM performance. The discrepancies also point out the importance of experimental evaluation of these techniques within the limitations of actual component performance.

3.2 Waveform Performance with Scintillation Playback

PER performance at 40 Msym/s was then characterized as a function of optical power for three scintillation profiles corresponding to $\sigma_I^2 = 0.2, 0.6,$ and 1.25 . Unlike the error response without scintillation which is influenced primarily by uncorrelated bit errors due to photodetector and front-end amplifier noise, the response with scintillation is correlated with the temporal period of atmospheric scintillation which can produce large fades lasting for many thousands of bits,

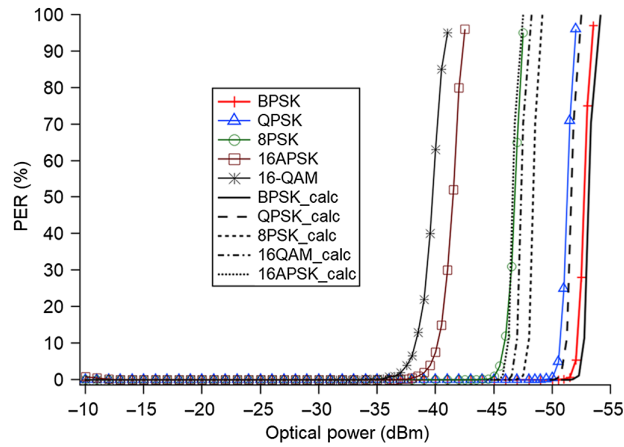


Fig. 4 Comparison of measured waveform performance to theoretical projections.

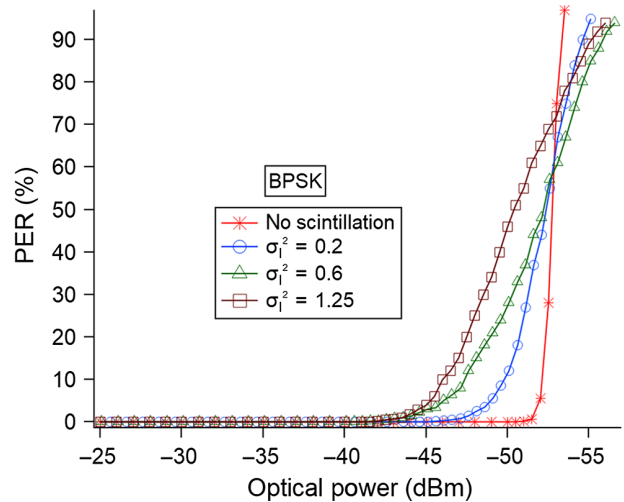


Fig. 5 BPSK PER measured as a function of optical power for scintillation file indices of 0.2, 0.6, and 1.25.

spanning multiple data packets. As such, PER is a more appropriate system performance figure of merit for atmospheric FSO links.^{29,34} Figures 5–9 show performance data for BPSK, QPSK, 8PSK, 16APSK, and 16-QAM, respectively. As expected, the power required to maintain a certain quality of service for each waveform increases as the scintillation strength increases. When compared with the no scintillation case, the power penalty incurred at 1% PER can be determined for each waveform operating under a particular scintillation profile. For $\sigma_I^2 = 0.2$ or low scintillation, an additional 3.9 dB is required to maintain 1% PER for BPSK, QPSK, and 8PSK. 16APSK and 16-QAM require 2.9 dB additional power at $\sigma_I^2 = 0.2$. For $\sigma_I^2 = 0.6$ or moderate scintillation, 7.4 dB additional power is required at 1% PER for BPSK, QPSK, and 8PSK, while 16APSK and 16-QAM require 6.4 dB more power. Under the $\sigma_I^2 = 1.25$ profile, BPSK, QPSK, and 8PSK require 8 dB more power at 1% PER relative to the no scintillation case, while 16APSK and 16QAM require 7 dB more power. Tables 2–6 show the power penalties associated with each scintillation profile for BPSK, QPSK, 8PSK, 16APSK, and 16-QAM, respectively.

3.3 Impact of Adaptive Equalization on Waveform Performance

Adaptive equalizers have been routinely used for RF applications to mitigate receiver channel distortions caused not only by signal strength variation but also intersymbol interference due to

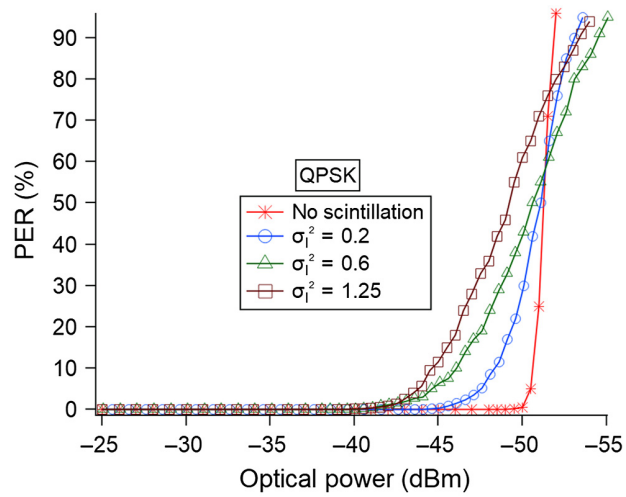


Fig. 6 QPSK PER measured as a function of optical power for scintillation file indices of 0.2, 0.6, and 1.25.

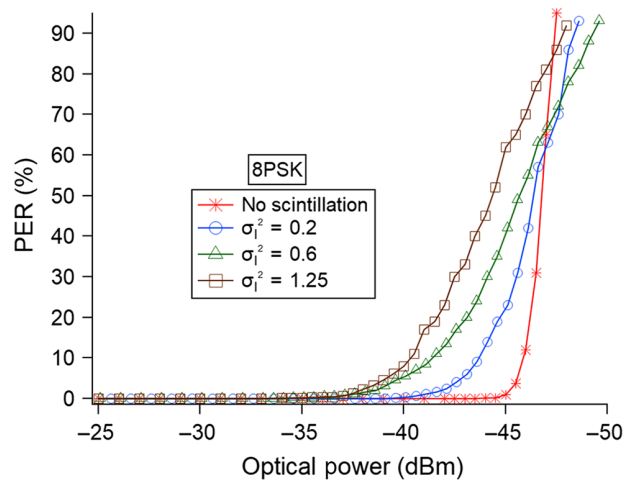


Fig. 7 8PSK PER measured as a function of optical power for scintillation file indices of 0.2, 0.6, and 1.25.

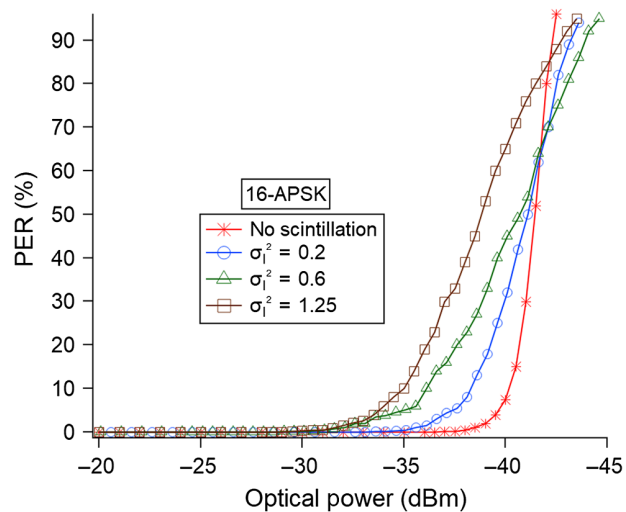


Fig. 8 16APSK PER measured as a function of optical power for scintillation file indices of 0.2, 0.6, and 1.25.

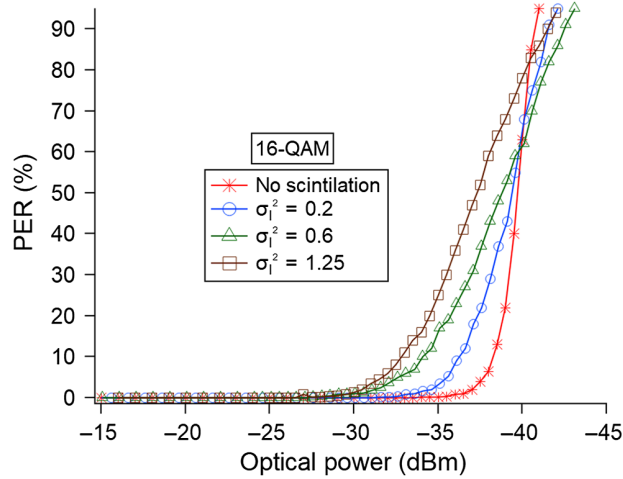


Fig. 9 16-QAM PER measured as a function of optical power for scintillation file indices of 0.2, 0.6, and 1.25.

Table 2 Optical power at 1% PER for each scintillation profile using BPSK waveform. Power penalty incurred for each scintillation profile as compared with the no scintillation case.

| Scintillation index (σ_I^2) | Optical power at 1% PER (dBm) | Scintillation power penalty (dB) |
|--------------------------------------|-------------------------------|----------------------------------|
| 0 | -51.5 | N/A |
| 0.2 | -47.6 | 3.9 |
| 0.6 | -44.1 | 7.4 |
| 1.25 | -43.5 | 8 |

Table 3 Optical power at 1% PER for each scintillation profile using QPSK waveform. Power penalty incurred for each scintillation profile as compared with the no scintillation case.

| Scintillation index (σ_I^2) | Optical power at 1% PER (dBm) | Scintillation power penalty (dB) |
|--------------------------------------|-------------------------------|----------------------------------|
| 0 | -50 | N/A |
| 0.2 | -46.1 | 3.9 |
| 0.6 | -42.6 | 7.4 |
| 1.25 | -42 | 8 |

Table 4 Optical power at 1% PER for each scintillation profile using 8PSK waveform. Power penalty incurred for each scintillation profile as compared with the no scintillation case.

| Scintillation index (σ_I^2) | Optical power at 1% PER (dBm) | Scintillation power penalty (dB) |
|--------------------------------------|-------------------------------|----------------------------------|
| 0 | -45 | N/A |
| 0.2 | -41.1 | 3.9 |
| 0.6 | -37.6 | 7.4 |
| 1.25 | -37 | 8 |

Table 5 Optical power at 1% PER for each scintillation profile using 16APSK waveform. Power penalty incurred for each scintillation profile as compared with the no scintillation case.

| Scintillation index (σ_I^2) | Optical power at 1% PER (dBm) | Scintillation power penalty (dB) |
|--------------------------------------|-------------------------------|----------------------------------|
| 0 | -38.5 | N/A |
| 0.2 | -35.6 | 2.9 |
| 0.6 | -32.1 | 6.4 |
| 1.25 | -31.5 | 7 |

Table 6 Optical power at 1% PER for each scintillation profile using 16-QAM waveform. Power penalty incurred for each scintillation profile as compared with the no scintillation case.

| Scintillation index (σ_I^2) | Optical power at 1% PER (dBm) | Scintillation power penalty (dB) |
|--------------------------------------|-------------------------------|----------------------------------|
| 0 | -36.5 | N/A |
| 0.2 | -33.6 | 2.9 |
| 0.6 | -30.1 | 6.4 |
| 1.25 | -29.5 | 7 |

multi-path effects. Since the impact of optical scintillation on an FSO receiver channel is similar, leveraging well-established adaptive equalization techniques was of interest in this research. There are multiple equalizer approaches that can be considered. Pilot or training sequence-based adaptive equalizers are very effective at compensating for time-varying channel distortions but require additional data overhead which limits data capacity. Blind adaptive equalizers use *a priori* statistical information of the transmitted data structure or format to adapt the equalization parameters to the incoming received signal through a constant modulus algorithm. Additional data overhead is not needed for a blind equalizer, but the convergence time is typically longer than that of training sequence-based approach.

Here, we implemented an IP core-compatible blind equalizer option from Silicon Infusion. While the data in Sec. 3.2 includes the performance benefit of the equalizer, this section highlights the performance difference with and without equalization using the $\sigma_I^2 = 0.2$ profile and compares it to a calculated PER response based on the fade probability for log-normally distributed irradiance.³⁵ Prior to implementing adaptive equalization, it was noted during characterization that the modem receiver was losing carrier lock despite having sufficient power relative to the sensitivity limit of the photodetector. As a result, the measured PER response without equalization exhibited diminished performance relative to the calculated response as shown in Fig. 10. After implementation of the blind equalizer, the PER response for each waveform was much more consistent with that predicted by log-normal statistics. For BPSK, QPSK, and 8PSK waveforms, the enhancement is ~ 1.5 dB at a 1% PER and > 2 dB at a PER $> 5\%$, which is of relevance when projecting coding gains for advanced forward-error-correction (FEC) techniques moving forward. The 16-QAM performance comparison shows minimal enhancement at 1% PER but a 1 to 1.5 dB improvement at 5% PER.

3.4 Predicting Waveform Availability for FSO-LEO Downlinks

Characterization of waveform performance under scintillation allows for more predictive link performance modeling for FSO links of interest such as FSO-LEO links. In this case,

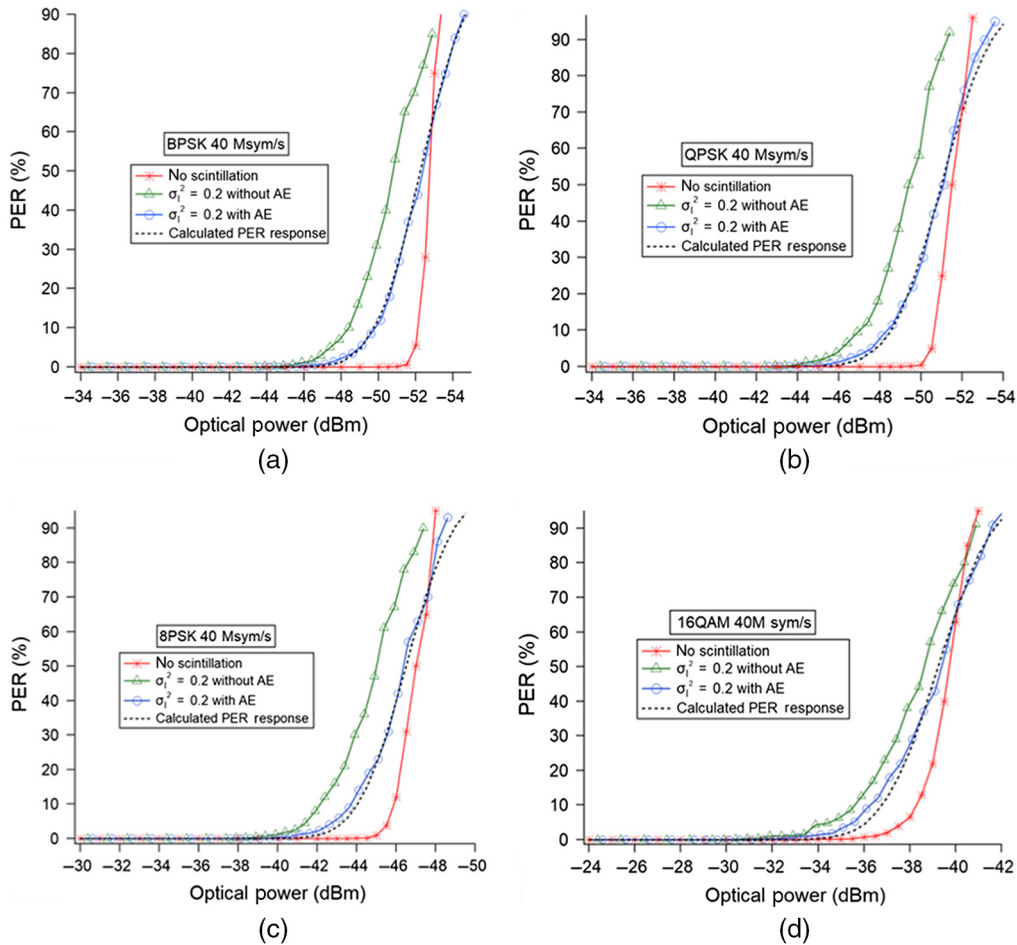


Fig. 10 Waveform performance with and without adaptive equalization, denoted as “AE” in the plot legends. Comparisons are shown between the measured PER response using a scintillation playback profile corresponding to $\sigma_I^2 = 0.2$ and the calculated response based on log-normally distributed irradiance for (a) BPSK, (b) QPSK, (c) 8PSK, and (d) 16QAM.

we consider an FSO-LEO downlink scenario where the space platform has a 5-cm transmit aperture, a 200 μ radian divergence, and a 2-W output power. The ground terminal has a 20 cm receive aperture in a high desert location with winter noon conditions. A space circular orbit with an 800-km altitude is assumed. Evaluating these parameters with the NRL-developed FOCAL link budget tool,³¹ we can first model scintillation index as a function of elevation angle. The modeled response, shown in Fig. 11, accounts for aperture averaging at the receiver, C_n^2 as a function of altitude, and scattering loss due to aerosols. We can then calculate average link power as a function of elevation angle as shown in Fig. 12. By merging the signal power and scintillation response with the waveform performance data, waveform availability can be predicted. In Fig. 12(a), waveform availability is mapped using waveform characterization data³³ taken prior to the performance improvements described in this paper. Figure 12(b) shows waveform availability for the same scenario but is now reevaluated using the current waveform performance data which includes power efficiency improvements for 4 bit/symbol waveforms discussed in Sec. 3.1 and waveform performance enhancements under scintillation discussed in Secs. 3.2 and 3.3. The waveform availability mapping for both cases is based on achieving a PER of 1% or less. Waveform availability based on current waveform performance shows continuous data coverage over the entire FSO-LEO pass. Furthermore, the use of a 4 bit/symbol waveform like 16APSK is not only viable for this link scenario but its availability now constitutes a predominant fraction of the LEO pass.

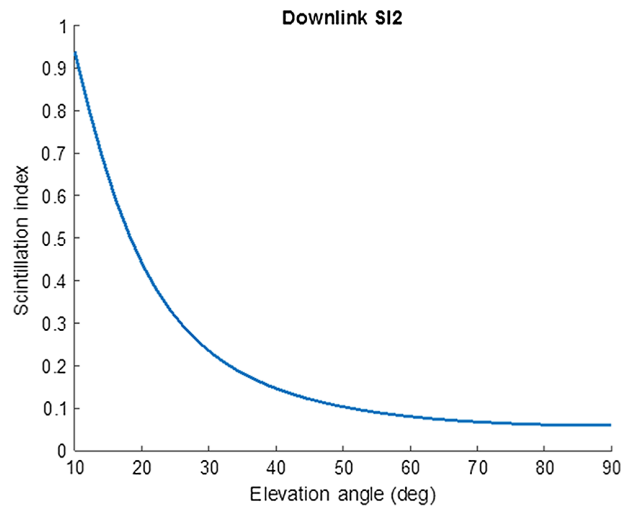


Fig. 11 Modeled scintillation index as a function of elevation angle for an FSO-LEO link scenario where the space platform has a 5-cm transmit aperture, a 200 μ radian divergence, and a 2-W output power. The ground terminal has a 20-cm receive aperture in a high desert location with winter noon conditions. At an 800-km altitude, space circular orbit is assumed.

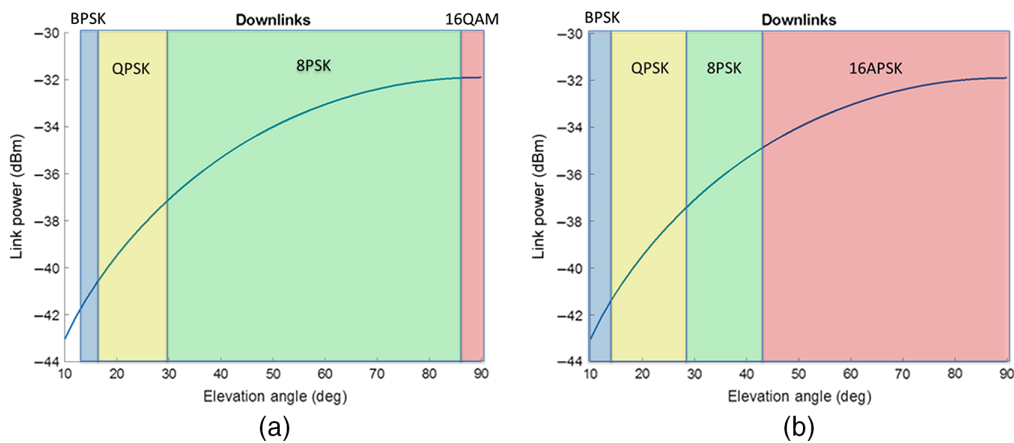


Fig. 12 Link power as a function of elevation angle for the FSO-LEO link scenario described in Fig. 10. Waveform availability was mapped using: (a) waveform performance data previously reported³³ and (b) current waveform performance data in Sec. 3.2.

4 Subcarrier Multiplexed System Development

As shown in Sec. 3, efficient bandwidth utilization can be achieved within a single 40-MHz modulation channel, but this only represents a fraction of the available bandwidth. Improving data throughput within the 165MHz detector bandwidth can involve increasing the signal channel symbol rate or implementing multiple modulation channels. Ideally, both approaches could be considered, but in this case, the single-channel symbol rate is limited by the modem hardware so a dual-channel modulation approach was investigated. The transmit architecture, shown in Fig. 13, was modified to support two 40-MHz modulation channels where the first channel is centered at 60 MHz and the second at 140 MHz. The two channels are combined through an RF diplexer, whose output is used to intensity modulate the laser transmitter. The transmitter is then attenuated via a VOA and coupled to the APD detector through a fiber focuser as shown in Fig. 14. A second diplexer is used to separate the APD’s output signal into separate channels where each channel is then sent to the waveform modem receiver for carrier and data recovery. Since both channels support a symbol rate of 40 Msym/s, the throughput supported by the dual-channel approach is double that of the single-channel case as shown in the inset table in Fig. 14.

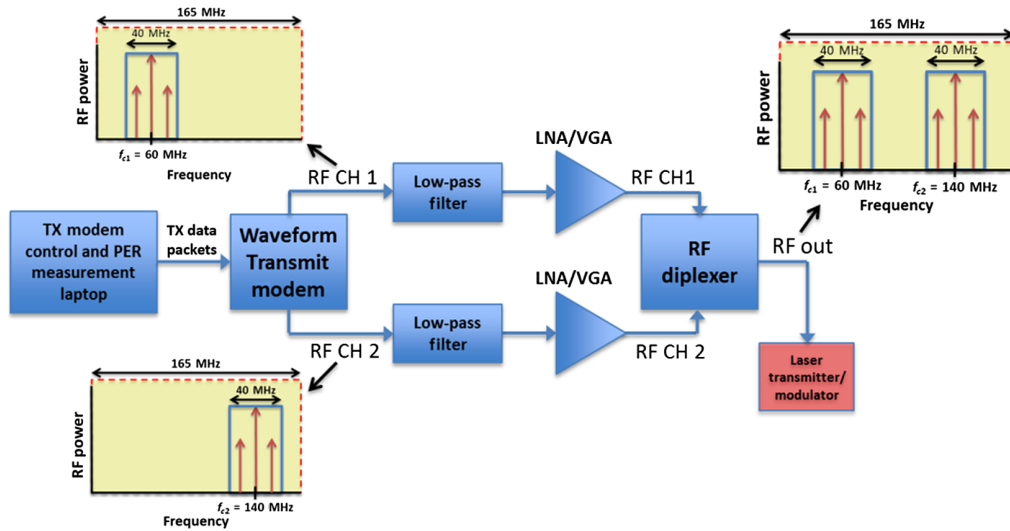


Fig. 13 A diagram of the transmit configuration for a dual-channel subcarrier multiplexed system. The first channel spans a 40-MHz bandwidth with a center carrier frequency of 60 MHz. The second channel spans a 40-MHz bandwidth with a center carrier frequency of 140 MHz. The output of the RF diplexer combines the frequency response of both modulation channels which is then imposed on the laser transmitter.

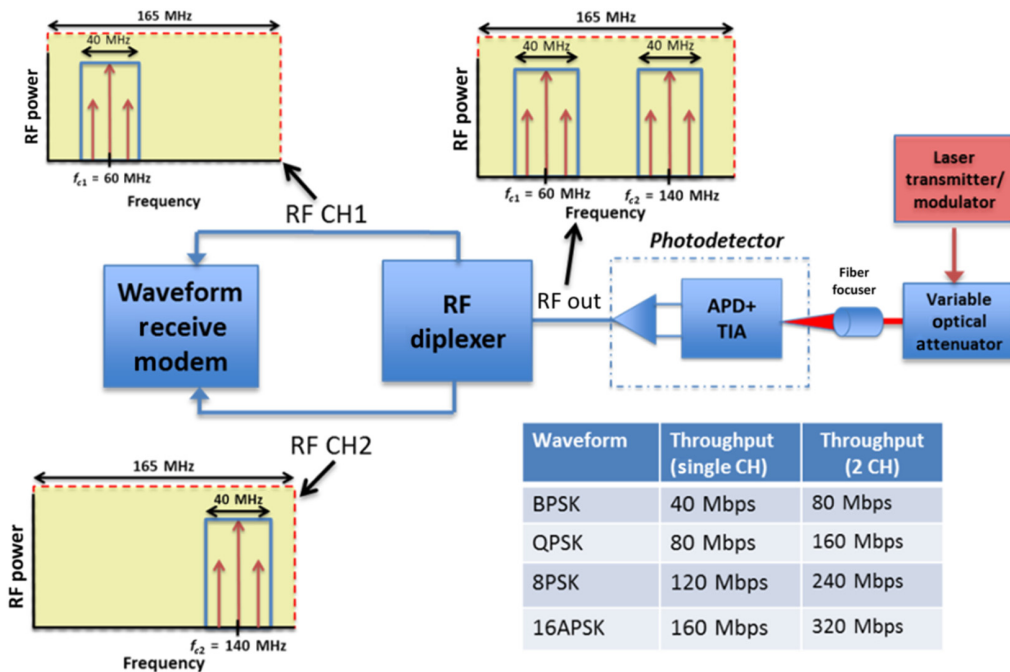


Fig. 14 A diagram of the receive configuration for a dual-channel subcarrier multiplexed system. The signal received by the APD includes the frequency response of both modulation channels. A diplexer is used to separate the signal into separate channels for carrier and data recovery at the receive modem. The lower right table inset shows the dual-channel throughput of the system, which doubles the throughput of the single-channel configuration described in Sec. 2.

For this initial characterization effort, waveform PER performance as a function of optical power was simultaneously measured for each modulation channel and compared with the single-channel response described in Sec. 3.1. Figure 15 shows the PER response of both channels in the dual-channel system relative to the single-channel case for BPSK, QPSK, 8PSK, and 16APSK waveforms. Given the 0.5 dB per channel effective insertion loss of the diplexers, some

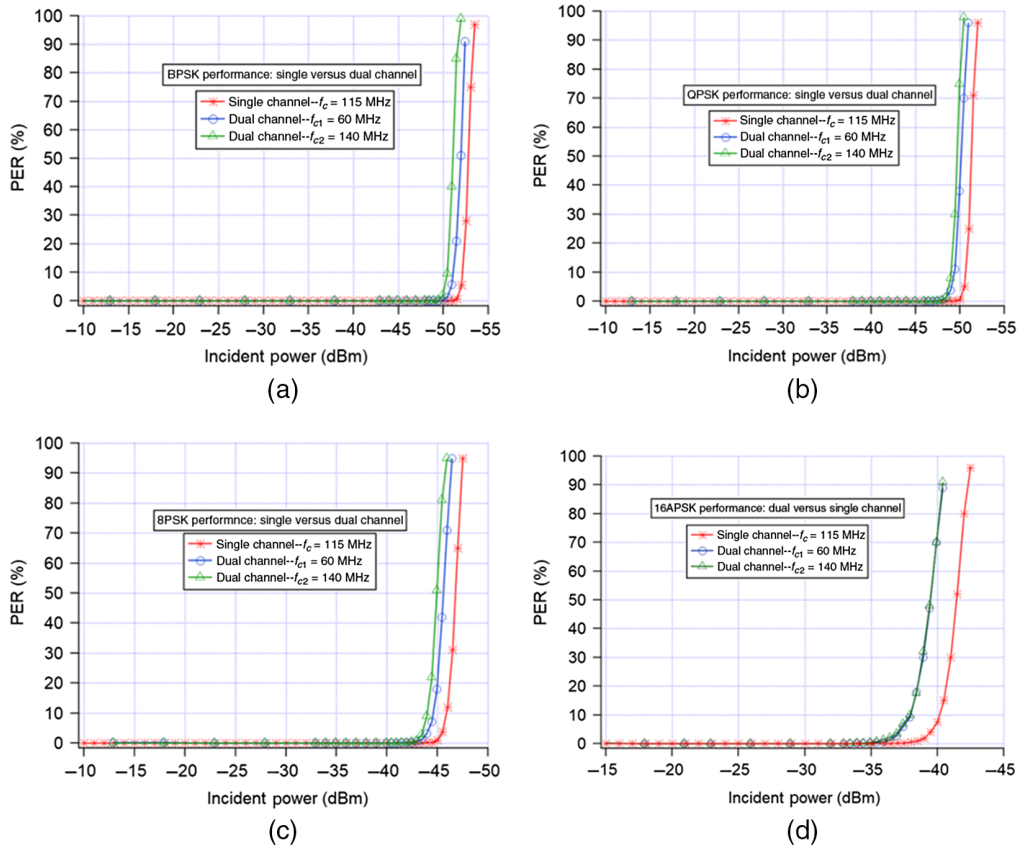


Fig. 15 Waveform performance comparison between single and dual-channel SIM system architectures for (a) BPSK, (b) QPSK, (c) 8PSK, and (d) 16APSK.

performance penalty is expected when comparing performance between the single and dual-channel configurations. When accounting for the losses through the diplexers, the performance of the dual-channel responses for BPSK and QPSK are within 1 dB of ideal performance as compared with single-channel performance. 8PSK and 16APSK are within 1.5 dB of ideal performance. Dual-channel 1% PER sensitivities for BPSK, QPSK, 8PSK, and 16APSK are -50.5 , -48.5 , -43 , and -36.5 dBm, respectively. As shown in Table 7, the throughputs supported by the dual-channel system are 80, 160, 240, and 320 Mbps for BPSK, QPSK, 8PSK, and 16APSK, respectively. With modest modem hardware improvements, the 165-MHz detector bandwidth could support two 60 Msym/s channels which would provide throughputs up to 480 Mbps. Furthermore, increasing the detector bandwidth would allow for both higher channel symbol

Table 7 Supported data throughput and optical power required to maintain 1% PER for BPSK, QPSK, 8PSK, and 16APSK waveforms for a dual-channel subcarrier multiplexed system with channel symbol rates of 40 Msym/s.

| Waveform | Dual-channel throughput (Mbps) | Optical power at 1% PER (dBm) |
|----------|--------------------------------|-------------------------------|
| BPSK | 80 | -50.5 |
| QPSK | 160 | -48.5 |
| 8PSK | 240 | -43 |
| 16APSK | 320 | -36.5 |

rates and a subcarrier multiplexed system that could be expanded beyond the two channels demonstrated here.

5 Conclusions

The time-varying atmospheric dynamics of FSO links can produce large changes in received signal power. Implementation of SIM waveforms allows for a bandwidth-efficient data transmission approach where the transmission waveform can be adapted to achieve higher data throughputs when signal power is high. We present continued research progress on the development of SIM waveform modems and the characterization of BPSK, QPSK, 8PSK, 16APSK, and 16-QAM waveform performance under various scintillation profiles using a laboratory scintillation playback system. Advancements include power efficiency improvements of higher-order waveforms such as 16APSK and waveform performance enhancements under scintillation through the implementation of adaptive equalization. The characterization results were used to model waveform availability for LEO downlink scenarios using an NRL-developed link budget tool. Last, a subcarrier multiplexed system was developed to improve throughput performance within the bandwidth of our photodetector. Characterizing the performance of this system with scintillation playback will be an area of interest moving forward. Future development also includes improving higher-order waveform performance via predistortion techniques, increasing single-channel modulation symbol rates and investigating advanced error-correction techniques in tandem with SIM waveforms.

Acknowledgments

We acknowledge the support of the Office of the Secretary of Defense.

References

1. R. Mahon et al., "Comparison of maritime measurements of C_n^2 with NAVSLaM model predictions," *Appl. Opt.* **59**, 10599–10612 (2020).
2. W. S. Rabinovich et al., "Estimation of terrestrial FSO availability," *Proc. SPIE* **10524**, 105240K (2018).
3. I. B. Djordjevic, "Adaptive modulation and coding for free-space optical channels," *IEEE/OSA J. Opt. Commun. Networking* **2**(5), 221–229 (2010).
4. A. J. Goldsmith and S. G. Chua, "Adaptive coded modulation for fading channels," *IEEE Trans. Commun.* **46**(5), 595–602 (1998).
5. W. G. Cowley, K. D. Nguyen, and D. Giggenbach, "Adaptive symbol-rate free-space-optical communications," in *Aust. Commun. Theory Workshop (AusCTW)*, pp. 122–127 (2013).
6. D. Giggenbach et al., "Space communications protocols for future optical satellite downlinks," in *Int. Astron. Congr. (IAC)* (2011).
7. F. Moll and M. Knapel, "Free-space laser communications for satellite downlinks: measurements of the atmospheric channel," in *Int. Astron. Congr. (IAC)* (2011).
8. D. Giggenbach et al., "System aspects of optical LEO-to-ground links," *Proc. SPIE* **10562**, 105625N (2017).
9. A. Shrestha and D. Giggenbach, "Variable data rate for optical low-Earth-orbit (LEO) downlinks," in *Photonic Networks; 17. ITG-Symp.; Proc.*, Leipzig, pp. 1–5 (2016).
10. D. Giggenbach, J. Horwath, and M. Knapel, "Optical data downlinks from Earth observation platforms," *Proc. SPIE* **7199**, 719903 (2009).
11. V. W. S. Chan, "Free-space optical communications," *J. Lightwave Technol.* **24**(12), 4750–4762 (2006).
12. M. K. Cheng et al., "Implementation of a coded modulation for deep space optical communications," in *IEEE Globecom 2006*, San Francisco, California, pp. 1–5 (2006).
13. W. Huang et al., "Atmospheric optical communication system using subcarrier PSK modulation," in *Proc. ICC '93 - IEEE Int. Conf. Commun.*, Vol. 3, pp. 1597–1601 (1993).

14. M. S. Ferraro et al., "Characterization of multi-level digital waveforms for low-Earth-orbit free space optical communication," *Proc. SPIE* **11678**, 1167814 (2021).
15. D. Giggenbach and F. Moll, "Scintillation loss in optical low earth orbit data downlinks with avalanche photodiode receivers," in *IEEE Int. Conf. Space Opt. Syst. and Appl. (ICSOS)*, pp. 115–122 (2017).
16. M. W. Wright et al., "LEO-to-ground optical communications link using adaptive optics correction on the OPALS downlink," *Proc. SPIE* **9739**, 973904 (2016).
17. M. S. Ferraro et al., "Position sensing and high bandwidth data communication using impact ionization engineered APD arrays," *IEEE Photonics Technol. Lett.* **31**(1), 58–61 (2019).
18. J. W. Rabinovich et al., "Effects of combinatorial sensing on tracking algorithms for FSO systems," *Proc. SPIE* **11272**, 112721J (2020).
19. R. You and J. M. Kahn, "Average power reduction techniques for multiple-subcarrier intensity-modulated optical signals," *IEEE Trans. Commun.* **49**(12), 2164–2171 (2001).
20. T. Darcie, "Subcarrier multiplexing for multiple-access lightwave networks," *J. Lightwave Technol.* **5**(8), 1103–1110 (1987).
21. W. O. Popoola and Z. Ghassemlooy, "BPSK subcarrier intensity modulated free-space optical communications in atmospheric turbulence," *J. Lightwave Technol.* **27**(8), 967–973 (2009).
22. J. Li et al., "Optical communication using subcarrier PSK intensity modulation through atmospheric turbulence channels," *IEEE Trans. Commun.* **55**(8), 1598–1606 (2007).
23. X. Song et al., "BER of subcarrier MPSK and MDPSK systems in atmospheric turbulence," *J. Lightwave Technol.* **33**(1), 161–170 (2015).
24. Q. Lu, Q. Liu, and G. S. Mitchell, "Performance analysis for optical wireless communication systems using subcarrier PSK intensity modulation through turbulent atmospheric channel," in *IEEE Global Telecommun. Conf., 2004. GLOBECOM '04*, Vol. 3, pp. 1872–1875 (2004).
25. B. Barua and S. P. Majumder, "Free space optical communication with OOK and BPSK modulation under different turbulent condition," in *Int. Conf. Inf., Electron. and Vision (ICIEV)*, Dhaka, pp. 1–5 (2013).
26. Y. Li et al., "Performance analysis of OOK, BPSK, QPSK modulation schemes in uplink of ground-to-satellite laser communication system under atmospheric fluctuation," *Opt. Commun.* **317**, 57–61 (2014).
27. L. C. Andrews and R. L. Phillips, *Laser Beam Propagation Through Random Media*, SPIE Press, Bellingham, Washington (2005).
28. S. Rajbhandari et al., "Experimental error performance of modulation schemes under a controlled laboratory turbulence FSO channel," *J. Lightwave Technol.* **33**(1), 244–250 (2015).
29. W. S. Rabinovich et al., "Characterization of modems and error correcting protocols using a scintillation playback system," *Proc. SPIE* **9739**, 97390M (2016).
30. M. S. Ferraro et al., "FSO links using high sensitivity gigabit combinational sensors and an adaptive high-throughput error-correction protocol," *Proc. SPIE* **10524**, 1052408 (2018).
31. W. S. Rabinovich et al., "Analysis of free space optical (FSO) communications and networking using adaptive waveforms for LEO satellites," *Proc. SPIE* **11272**, 112720D (2020).
32. M. S. Ferraro et al., "Impact-ionization-engineered avalanche photodiode arrays for free-space optical communication," *Opt. Eng.* **55**(11), 111609 (2016).
33. M. S. Ferraro et al., "Advanced digital waveforms for low-Earth-orbit (LEO) FSO links," *Proc. SPIE* **11272**, 112720A (2020).
34. W. S. Rabinovich et al., "Scintillation recording and playback in free-space optical links," *Opt. Eng.* **55**(11), 111613 (2016).
35. F. S. Vetelino, C. Young, and L. Andrews, "Fade statistics and aperture averaging for Gaussian beam waves in moderate-to-strong turbulence," *Appl. Opt.* **46**, 3780–3789 (2007).

Biographies of the authors are not available.